DEVELOPMENT OF HIGH SPECIFIC SPEED MIXED FLOW COMPRESSORS

by
Fumikata Kano
Yoshiteru Fukao
and
Takafumi Shirakami
Mechanical Engineering Research Lab
Kobe Steel, Limited
Kobe, Japan

Fumikata Kano has been an Engineer at Kobe Steel, Limited, in Kobe, Japan, for more than twenty years. He has been in the management of turbomachinery design, development and research since 1976. He is currently in turbomachinery development in the Mechanical Engineering Research Lab. A member of the ASME, Mr. Kano received a B.S. in Mechanical Engineering from Osaka City University.

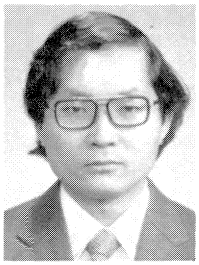

Yoshiteru Fukao has been with the Mechanical Engineering Research Lab at Kobe Steel, Limited, Kobe, Japan, since 1978. He has been developing and designing turbomachinery for seven years. He received an M.S. degree in Mechanical Engineering from Osaka University.

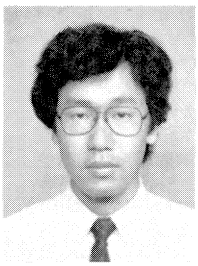

Takafumi Shirakami joined Kobe Steel, Limited, in Kobe, Japan in 1981. He is engaged in the development of turbomachinery as an Engineer in the Mechanical Engineering Research Lab. He received an M.S. degree in Mechanical Engineering from Osaka University.

ABSTRACT

The results of a study on the aerodynamic performance of a high specific speed, mixed flow compressor are presented. The specific speed was $N_s = 450$ to 550 $(m^3/min)^{1/2}$ (rpm) $(m^{-3/4})$, with approximately a 2.0 pressure ratio per stage. The flow path from the outlet of the mixed flow impeller was inclined in the axial direction and entered into a curved diffuser. A theoretical flow analysis and a performance test were performed. The slip factor for this type of compressor should be predicted by a different formula from that used for centrifugal compressors. Distributions of the flow velocity, temperature and pressure were measured, using a highly sensitive pressure transducer and a total temperature probe. The flow field, including the end wall boundary layer, was surveyed. The losses and the flow condition of the unsteady flow were analyzed. The compressor of $N_s = 450$ to 500 showed high efficiency and handled a flowrate of about twice as much as a conventional centrifugal compressor. This development contributes tremendously in reducing the compressor size.

INTRODUCTION

In comparison with the conventional centrifugal compressor of the same stage pressure ratio, the specific speed of the developed mixed flow compressor is 1.5 times as large as the value for a conventional compressor. The flowrate of the new compressor is twice as much as a conventional compressor utilizing the same impeller diameter. This can reduce the size of the compressor, which contributes to lower costs for compressors and their facilities. These compressors are used in various applications, such as air and mixed gas compressors, and in the power range from 100 kW to 30 MW with single or multiple stages.

This mixed flow compressor was developed by investigating the aerodynamic performance and impeller stress. The flow analysis in the high specific speed impeller and the unsteady flow analysis in the diffuser were very important. The flow was strongly influenced by the impeller blading and influences the performance of the stationary vanes located downstream of the impeller. A thorough study of the unsteady flow in the curved diffuser after the mixed flow impeller was performed. A 22,000 m^3/h mixed flow compressor of this design is in operation.

SPECIFIC SPEED AND COMPRESSOR SIZE

The size of a compressor can be reduced significantly by using a high specific speed impeller. The specific speed, N_s, is represented by sevearl formulas in accordance with their appropriate applications. The formula for N_s is represented as follows, using the suction flowrate at the impeller inlet:

$$N_s = \frac{N\,(Q_1^{0.5})}{H^{0.75}} \qquad (1)$$

A comparison of the compressor sizes for single-stage compressors is illustrated in Figure 1. These two compressors were designed for the same specifications. One was designed as a usual centrifugal compressor of $N_s = 330$, while the other design was a mixed flow compressor of $N_s = 450$. The impeller and the casing diameters were reduced by 20 percent. By reducing the size and weight of the impeller, smaller sized shaft bearings may be utilized for the overhung type compressor. The difference in the compressor weight between the $N_s = 450$ design and the $N_s = 330$ design becomes large with

increasing flowrate. This is very important to reduce the manufacturing and operation costs. A comparison of the compressor weight and size is shown in Figure 2. Photographs of the $N_s=330$ impeller and $N_s=450$ impeller are shown in Figures 3 and 4, respectively.

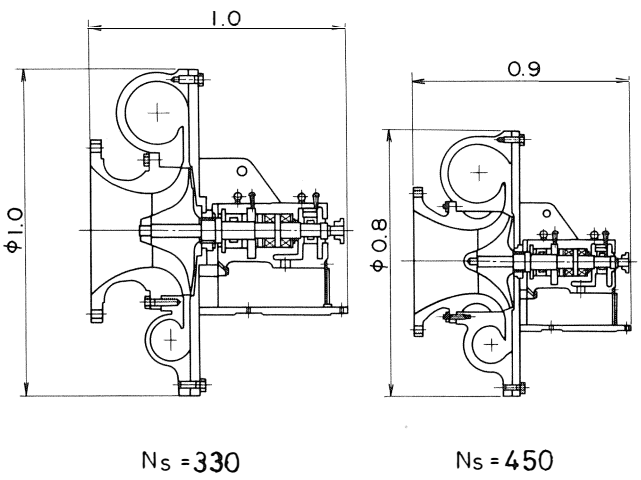

Figure 1. Comparison of Compressor Size.

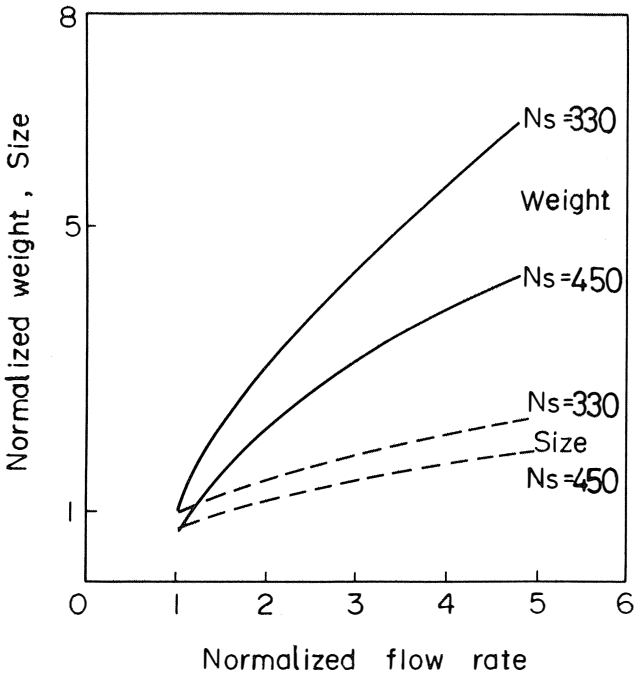

Figure 2. Reduction of Size and Weight of Compressor.

OPTIMIZATION OF IMPELLER INLET

The first step of a one-dimensional design is the optimization of the inlet shape of the impeller blade. One of the most important factors to maintain high efficiency and wide operation range is to minimize the relative velocity at the inducer tip. The following relationships were derived from the inlet velocity vector triangle, under the condition of minimum relative velocity. Pre-swirl of the flow was considered zero.

The optimum inducer tip diameter, relative velocity and blade angle were determined by the following formulas:

$$\left(\frac{D_{1t}}{D_2}\right)_{opt}=\sqrt{1.26\left(\frac{\phi_1}{1-BL}\right)^{2/3}+\left(\frac{D_{1h}}{D_2}\right)^2} \tag{2}$$

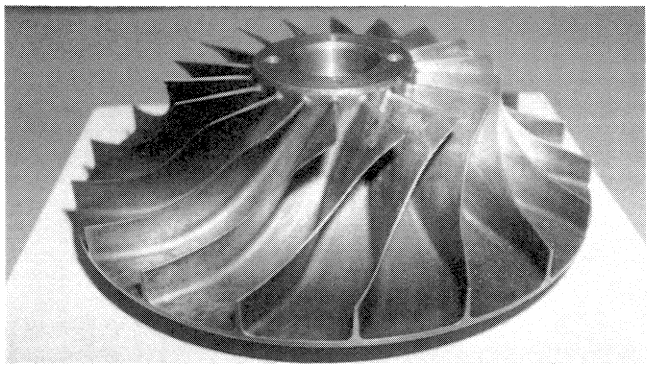

Figure 3. Impeller, $N_s=330$.

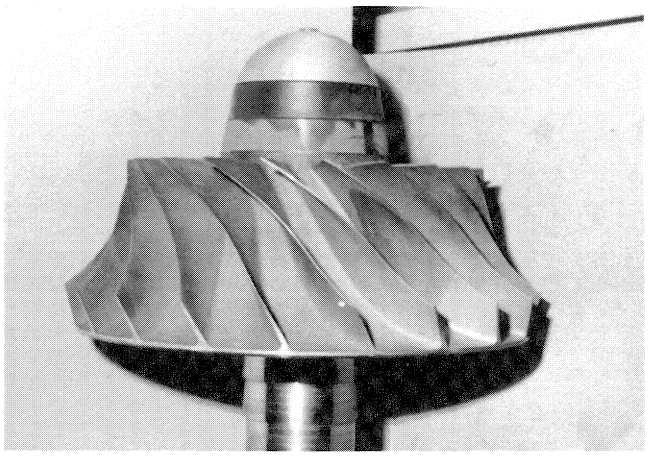

Figure 4. Impeller, $N_s=450$.

$$\left(\frac{w_{1t}}{U_2}\right)_{opt}=\left[\frac{\phi_1}{\left[\left(\frac{D_{1t}}{D_2}\right)^2_{opt}-\left(\frac{D_{1h}}{D_2}\right)^2\right](1-BL)}\right]^2+\left(\frac{D_{1t}}{D_2}\right)^2_{opt} \tag{3}$$

$$\left(\beta_{1t}\right)_{opt}=\cos^{-1}\left\{\frac{\left(\frac{D_{1t}}{D_2}\right)_{opt}}{\left(\frac{w_{1t}}{U_2}\right)_{opt}}\right\} \tag{4}$$

where ϕ_1 is the flow coefficient,

$$\phi_1=\frac{Q_1}{\frac{\pi}{4}D_2{}^2\,U_2} \tag{5}$$

The inlet absolute velocity is assumed to be uniform from the hub to the shroud.

The calculation results concerning the inlet optimization are shown in Figures 5, 6 and 7. The optimum blade angle β_{1t} is approximately constant for a fairly wide range of the flow coefficient. The specific speed was selected primarily using these charts.

OPTIMIZATION OF IMPELLER EXIT

In the meridional flow path (Figure 8), the curvature of the shroud side is most important from the standpoint of boundary layer separation. Simplified calculation results are shown in Figure 9 for the shroud line curvature and the exit flow angle in the meridional plane. The shroud side curvature was considered one continuous circular arc. The diameter De is the diameter at which the curvature of the diffuser wall terminates. Considering a constant value for Rs/D_2, the higher

the specific speed, the larger the ratio De/D_2 becomes and the smaller the exit pitch angle becomes, as shown in Figure 9.

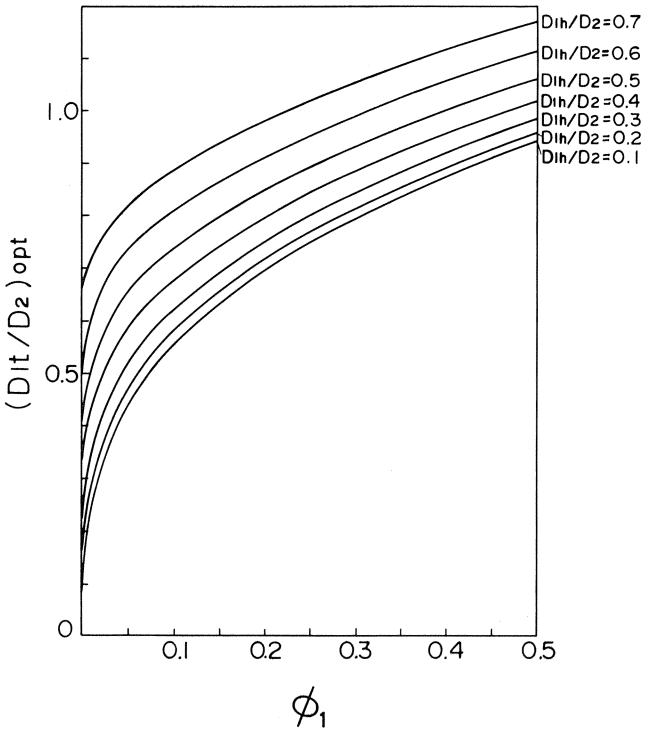

Figure 5. Optimum Inducer Tip Diameter of Impeller.

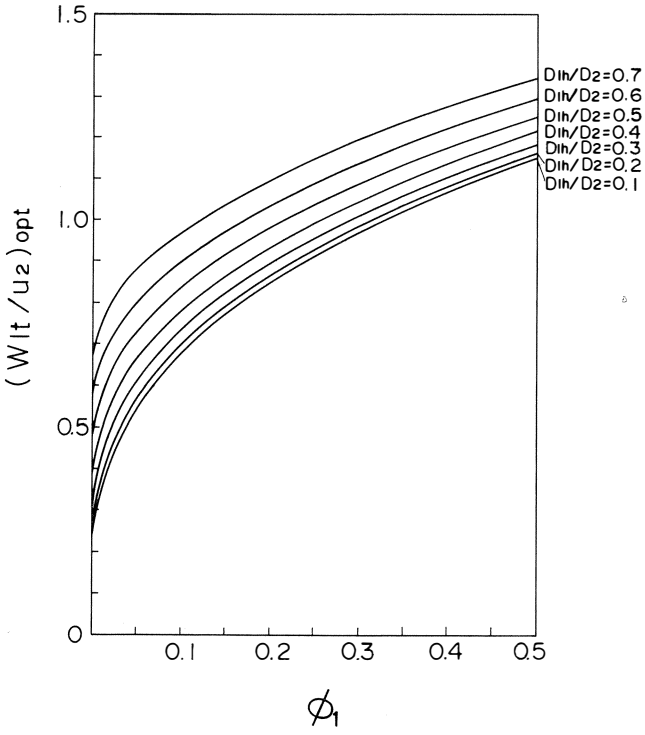

Figure 6. Optimum Relative Velocity at Inducer Tip.

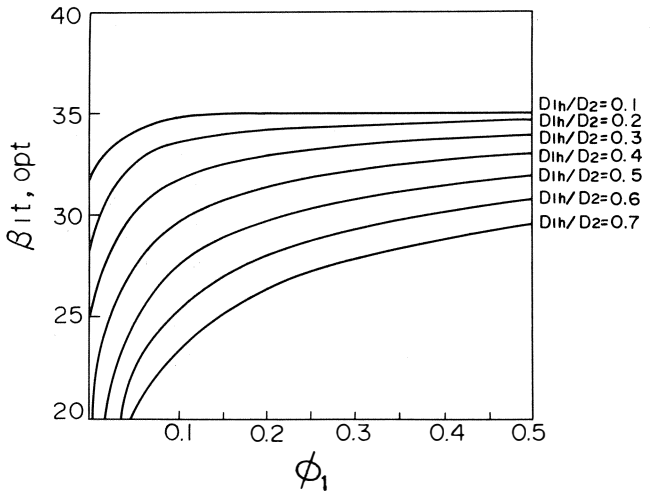

Figure 7. Optimum Blade Angle at Inducer Tip.

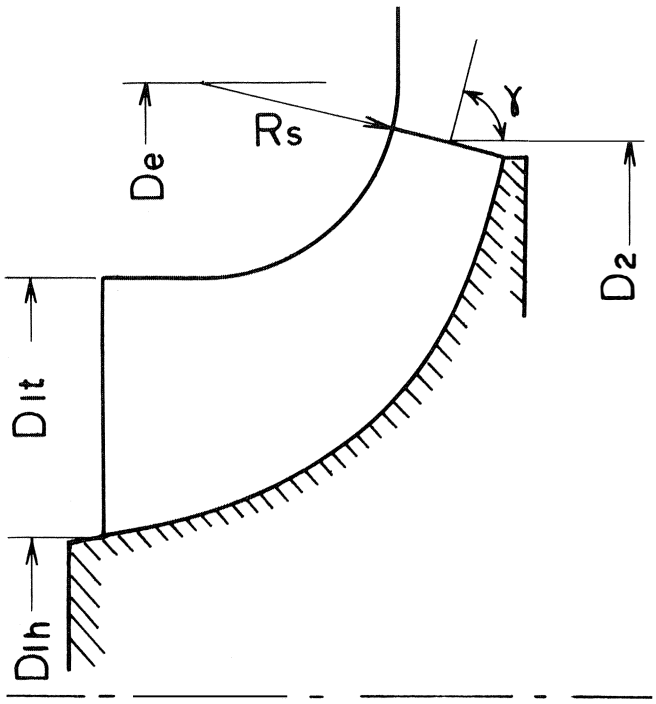

Figure 8. Meridional Plane of Mixed Flow Compressor.

The theoretical head is represented by the following relation:

$$H_{th} = \frac{1}{g} U_2^2 \left(\frac{Cu_2}{U_2} - \frac{U_1 Cu_1}{U_2^2} \right) \quad (6)$$

In many cases, where pre-swirl at the inlet is zero, the quantity Cu_2/U_2 is the most influential factor. This quantity is determined using the slip factor and the velocity vector triangle. The slip factor applicable to the mixed flow impeller was represented by modifying the Stodola equation with the following considerations:

- The relative circulation flow in the blade-to-blade flow path of the impeller is reduced in accordance with the decrease of the diagonal pitch angle in the meridional plane. This was modified by sin γ.
- The separated flow or the thick boundary layer varies the exit flow angle and the width of the flow path.

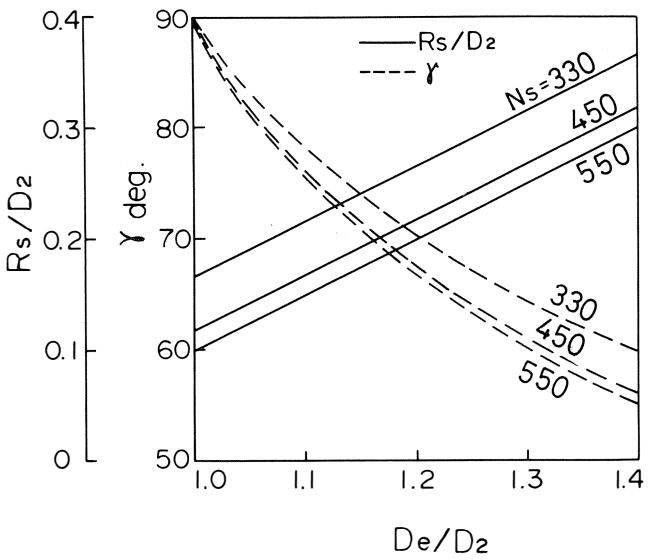

Figure 9. Shroud Side Curvature and Pitch Angle.

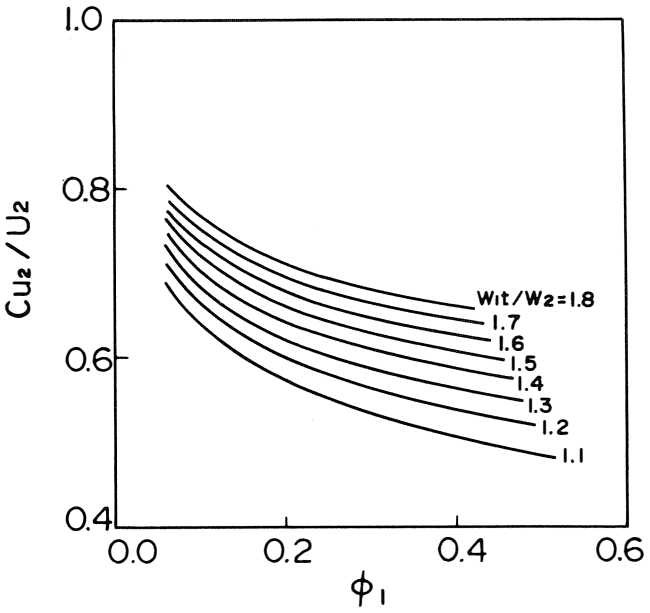

Figure 10. Value of Cu_2/U_2.

• The relative velocity deceleration mainly affects the boundary layer thickness or the flow separation.

• The relative circulation is represented more appropriately by applying the "f" factor.

The slip factor is predicted by the following formula:

$$\mu = \frac{H_{th}}{H_{th\infty}} = \frac{1 - \frac{Cm_2}{U_2}\cot\beta_{2_{corr}} - f\frac{\pi}{Z}\sin\beta_{2_{corr}}\sin\gamma\,(1-\epsilon)}{1 - \frac{Cm_2}{U_2}\cot\beta_2}$$

where

$$f = \frac{1}{2}\int_{(\beta_2 - \frac{\pi}{2})}^{(\beta_2 + \frac{\pi}{2})} \sin\theta\cdot\sin(\theta + \tfrac{\pi}{2} - \beta_2)d\theta \qquad (7)$$

The slip factor can be converted into the quantity Cu_2/U_2 using the following relationship:

$$S = Cu_2/U_2 = \mu\left(1 - \frac{Cm_2}{U_2}\cot\beta_2\right) \qquad (8)$$

This quantity was used for the one-dimensional optimization, and is shown in Figure 10 with parameters of the relative velocity deceleration in the flow path. In the case of the high specific speed impeller, the head produced by centrifugal force was less than the head expected from a similarly operated low specific speed impeller. The quantity S becomes small when the flow coefficient is large and the velocity deceleration is small. Large relative velocity deceleration is necessary to obtain a high head, but should be carefully determined for the case of the high specific speed impeller, because of its three-dimensional flow. The important items which should be taken into consideration are the velocity flow distribution in the impeller and the flow condition at the diffuser inlet.

THREE-DIMENSIONAL DESIGN OF IMPELLER

Specifications for high specific speed mixed flow impellers which have large inlet hub diameters are shown in Table 1. The impellers H1, H2 and H3 have the same specific speed, but each has a different flow velocity distribution. In this table, the specification of a centrifugal impeller, C1, is also shown for comparison to the mixed flow impellers. All of the impellers were unshrouded.

Table 1. Parameters of tested impellers.

Parameters \ Impeller	H1	H2	H3	H4	H5	C1
Diagonal pitch angle in the meridional plane, deg.	65.0	65.0	65.0	65.0	65.0	90.0
Specific speed, $(m^3/min)^{1/2}\cdot rpm\cdot m^{-3/4}$	450	450	450	500	550	330
Mean exit diameter of impeller, mm	381	381	381	342	342	250
Mean exit blade angle of impeller, deg.	65.0	65.0	60.0	60.0	63.0	60.0
Relative velocity deceleration ratio, w_{1t}/w_2	1.45	1.61	1.63	1.72	1.65	1.81

The blade geometry was specified in terms of straightline elements, as illustrated in Figure 11. The blade was initially designed using a quasi-three-dimensional flow analysis to the point where it was fairly close to the final geometry. A three-dimensional boundary layer calculation was also performed to refine the design.

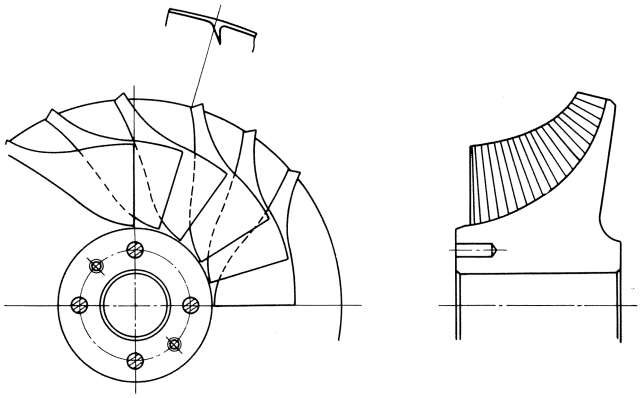

Figure 11. Mixed Flow Impeller, H3.

The angular momentum of the fluid in the impeller increases linearly from the inlet to the exit. All of the impellers had similar angular momentum distributions, as shown in Figure 12. Because the streamline in the meridional plane of the high specific speed impeller is diagonal in the entire flow path, it was rather easy to provide a blade geometry to meet the angular momentum distribution which increases linearly. The angular momentum increase is closely related to the blade angle distribution, shown in Figure 13.

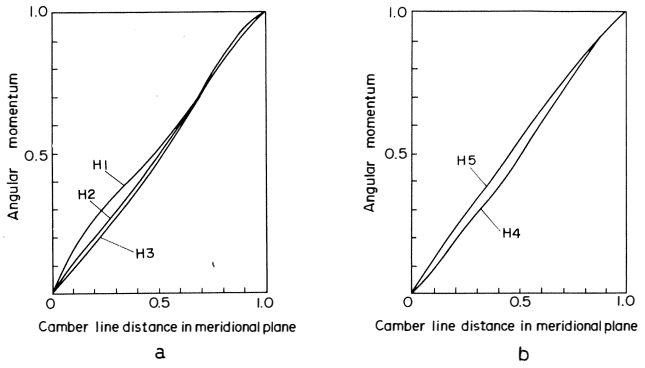

Figure 12. Angular Momentum in Mixed Flow Impeller.

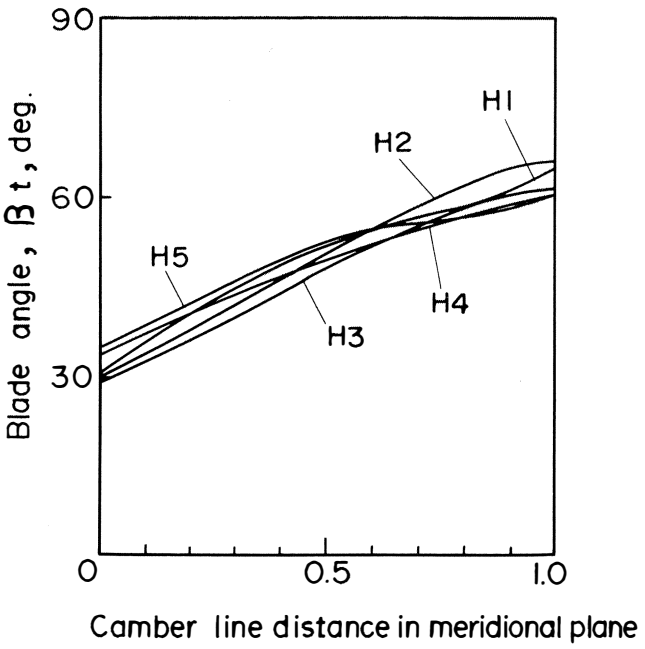

Figure 13. Blade Angle Distribution.

The high specific speed impeller has somewhat different blade characteristics in comparison with those of an ordinary centrifugal compressor impeller (C1), as shown in Figure 14. The difference in the momentum increase between the mixed flow impeller and the centrifugal impeller exists in the first half of the flow path. In the case of the centrifugal compressor, light loading is favorable to avoid the rapid increase in the thickness of the boundary layer which causes large flow separation due to Coriolis forces in the latter half of the flow path. The Coriolis force is reduced due to the diagonal pitch angle in the latter half of the flow path of the mixed flow impeller, allowing the inducer to be loaded moderately.

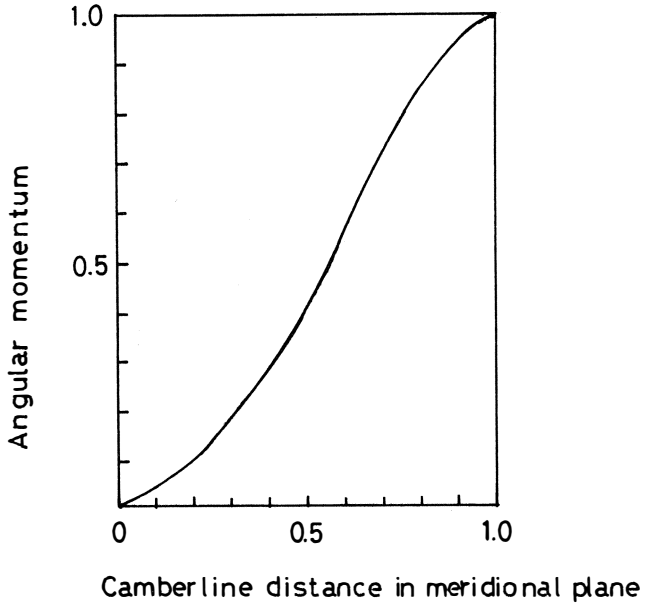

Figure 14. Angular Momentum in Centrifugal Impeller, C1.

The blade thickness was determined after examination of the stresses caused by rotation and aerodynamic considerations. The blade was relatively thinner at the inducer than any other part, and was thicker at the base than at the tip.

DIFFUSER

A curved diffuser followed the mixed flow impeller. The first portion of the diffuser was vaneless. From the terminal radius of the wall curvature, a straight parallel wall extended in the radial direction. Diffuser vanes were located in this straight section. The velocity distribution at the leading edge of a diffuser vane is important to maintain good diffuser performance by eliminating the incidence loss. Even though a curved diffuser tends to twist the flow distribution, it was necessary to design the curved diffuser to get the same level of flow distortion that exists in a straight diffuser at the leading edge of the diffuser vane.

The curvature of the walls was determined after elemental tests were performed for several curvatures. These tests utilized the swirl flow generated by stationary swirl vanes instead of an impeller. The curved diffusers were formed with a single circular arc. The ratio of the shroud side to hub side wall curvature was 2.0, and the curvatures terminated at a radius of 1.16 times of the impeller mean exit radius. The diffuser width was set to be $b_e/b_2 = 0.91$.

EXPERIMENTAL FACILITY AND MEASUREMENTS

A sectional view of the test rig of a mixed flow compressor is shown in Figure 15. The external surface of the compressor casing was covered with a 100 mm thick insulation material to eliminate the heat leakage effect on the total temperature. This facility was driven by an electric motor through a speed increasing gear. The air flowed through a straightener at the inlet of the compressor. The inlet conditions were almost the same as ambient conditions. The tests were performed for five impellers with vaneless diffusers. Diffuser vanes were provided only for the impeller H3. The test of the centrifugal compressor C1 was also performed by a similar method. The measurements obtained were as follows:

• Static pressure and total pressure distributions at the impeller exit. These were measured by a three-hole cobra probe at the positions of $r/r_2 = 1.03$, 1.08, 1.14, 1.16, 1.39 and 1.69.

• Unsteady total pressure variations were also taken at the above six radii. At each radius, the flow was surveyed across the entire passage at ten axial locations using a highly sensitive pressure transducer and a total temperature probe.

• Total pressure, static pressure and total temperature at the suction and discharge of the compressor.

• Discharge flowrate was determined utilizing an orifice meter.

The unsteady total pressure was measured for three directions at each location. From the data of the unsteady total pressure and the total temperature, values for the flow velocity, static pressure, static temperature, density and flow angle at each location were determined.

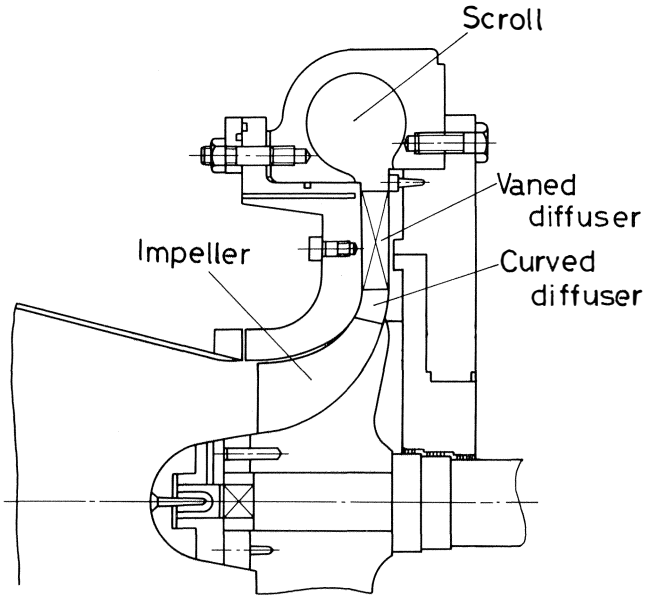

Figure 15. Sectional View of Test Facility.

IMPELLER PERFORMANCE

The efficiency at the design conditions of each impeller is shown in Figure 16. The maximum efficiency was obtained with a specific speed of 450. The efficiency at this point was 2.5 percent higher than the efficiency of the centrifugal compressor C1. The $N_2 = 550$ mixed flow compressor efficiency was the same as the $N_s = 330$ centrifugal compressor efficiency.

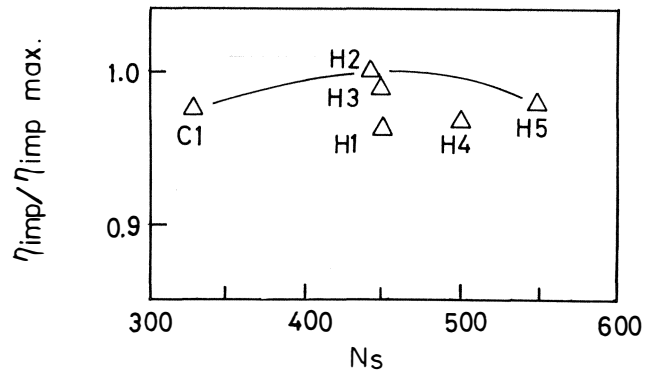

Figure 16. Impeller Efficiency.

The impeller H4 did not show the highest efficiency. It is presumed that the large velocity deceleration caused a thick boundary layer, which deteriorated the efficiency of the impeller.

Slip factors for the impellers are shown in Figure 17. The mixed flow impellers showed higher slip factors than the centrifugal impeller, due to the diagonal flow in the meridional plane. This high slip factor is very convenient for obtaining a high head impeller. The slip factor of impeller H4 was lower than the other mixed flow impellers, such as H2 and H3. The slip factor and the impeller efficiency are both influenced by low momentum fluid in the flow path. It may be presumed that the low slip factor and the relatively low impeller efficiency of impeller H4 are both related to the low quality of the three-dimensional blade shape.

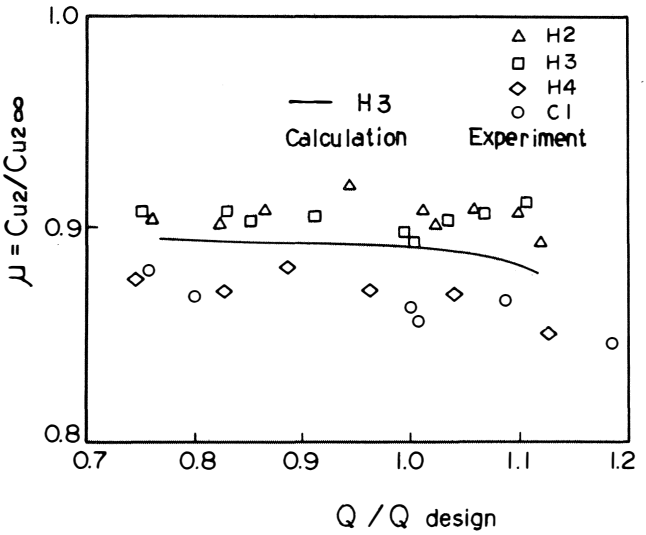

Figure 17. Slip Coefficient.

The slip factor during off-design conditions was not the same as that for design conditions. In many cases, the slip factor increased as the flowrate decreased. In the case of impeller H2, the reverse tendency, namely the slip factor at the small flowrates being lower than at the design condition, was evident. The relative velocity deceleration in the impeller may be greatly related to the flow deviation and the slip factor.

STAGE PERFORMANCE

The stage efficiency was also a maximum for the $N_s = 450$ compressor, as shown in Figure 18. This stage efficiency was

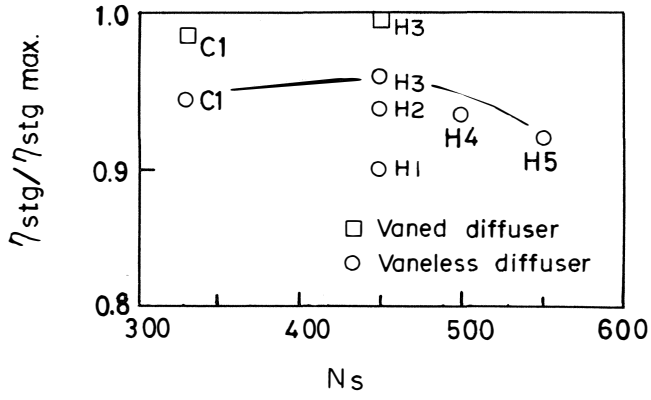

Figure 18. Stage Efficiency.

higher than the efficiency of compressor C1 ($N_s = 330$). Compressors designed utilizing specific speeds higher than 450 demonstrated an efficiency decrease at the design conditions. The efficiency at $N_s = 550$ was two percent lower than that of compressor C1. This is useful when considering that the high specific speed compressor handled more than twice the flowrate of compressor C1. The increase in efficiency due to the vaned diffuser was almost the same as the increase for the case of compressor C1.

FLOW DISTRIBUTION IN VANELESS DIFFUSER

Flow through the curved diffuser tended to cause separation at the convex wall. It is necessary to control the separation with suitable wall curvature and diffuser width variation. Further, it is important to provide the diffuser vane before the separation position in order to guide the flow smoothly.

The meridional velocity distributions in the curved vaneless diffuser, downstream of impeller H3, are shown in Figure 19 and are the results of measurements by the cobra probe. The values in Figure 19 were time-averaged with the blade-to-blade velocity distribution. This curved vaneless diffuser existed in the meridional plane to a radius ratio $r/r_2 = 1.16$. The flow did not separate in the region of the curved diffuser. At a radius ratio $r/r_2 = 1.39$, flow separation existed at the shroud side wall during low flowrate conditions. The separation occured in the region from $r/r_2 = 1.16$ to 1.39. It was, therefore, effective to provide diffuser vanes starting at a radius ratio $r/r_2 = 1.16$. The meridional velocity at the shroud side wall became very low in comparison to the hub side wall. This may be due to the wall curvature and the initial small flow angle at the impeller exit.

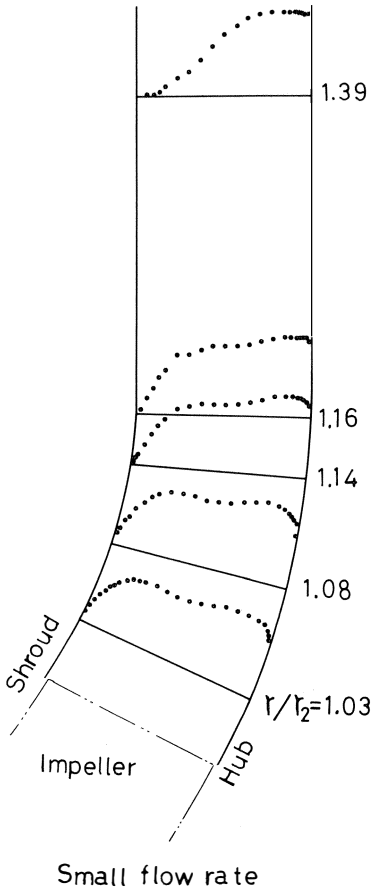

Figure 19. Velocity Distribution in Meridional Plane.

The unsteady flow at the outlet of the impeller became uniform in the vaneless diffuser. Theoretical analysis was performed to determine the conditions of the pressure and velocity fluctuations. The Navier-Stokes equation can be linearized, providing that the unsteady amplitude is sufficiently small in comparison with the mean value. This approach was applied to the curved diffuser.

The momentum equations in the direction along the meridional mean streamline and in the tangential direction are as follows, using relative coordinates that rotate at an angular velocity ω:

$$\begin{aligned}
&\bar{w}_m \frac{\partial}{\partial m}(\bar{w}_m \sin\gamma) + w_m' \frac{\partial}{\partial m}(\bar{w}_m \sin\gamma) + \bar{w}_m \frac{\partial}{\partial m}(w_m' \sin\gamma) \\
&\quad + \frac{\bar{w}_m}{\tan\gamma} \frac{\partial}{\partial m}(\bar{w}_m \cos\gamma) + \frac{\bar{w}_m}{\tan\gamma} \frac{\partial}{\partial m}(w_m' \cos\gamma) \\
&\quad + \frac{w_m'}{\tan\gamma} \frac{\partial}{\partial m}(\bar{w}_m \cos\gamma) + \frac{\bar{w}_u}{r}\left(\sin\gamma + \frac{\cos\gamma}{\tan\gamma}\right) \frac{\partial w_m'}{\partial\theta} - \frac{A^2}{r^3} \\
&\quad - \frac{2}{r^2} A w_u' \\
&= -\frac{1}{\rho} \frac{1}{\sin\gamma} \frac{\partial}{\partial m}\left[\bar{P}_0 - \frac{1}{2}\rho\left(\bar{w}_m^2 + (\bar{w}_u + r\omega)^2\right) + Ps'\right] \\
&\quad + \nu\left[\frac{1}{\sin\gamma}\left(1 + \frac{1}{\tan^2\gamma}\right) \frac{\partial^2(\bar{w}_m + w_m')}{\partial_m^2}\right. \\
&\quad + \frac{1}{r}\left(1 + \frac{1}{\tan^2\gamma}\right) \frac{\partial}{\partial m}(\bar{w}_m + w_m') + \frac{\sin\gamma}{r^2} \frac{\partial^2 w_m'}{\partial\theta^2} - \frac{\bar{w}_m}{r^2}\sin\gamma \\
&\quad \left. - \frac{w_m'}{r^2}\sin\gamma \frac{2}{r^2} \frac{\partial w_u'}{\partial_\theta} + \frac{1}{r^2\tan\gamma}\cos\gamma \frac{\partial^2 w_m'}{\partial_\theta^2}\right] \qquad (9)
\end{aligned}$$

$$\begin{aligned}
&\bar{w}_m \frac{\partial \bar{w}_u}{\partial m} + w_m' \frac{\partial \bar{w}_u}{\partial m} + \bar{w}_m \frac{\partial w_u'}{\partial m} + \frac{\bar{w}_u}{r} \frac{\partial w_u'}{\partial\theta} \\
&\quad + \frac{1}{r}\sin\gamma\left(\bar{w}_m \bar{w}_u + w_m' \bar{w}_u + \bar{w}_m w_u'\right) + 2\omega(\bar{w}_m + w_m')\sin\gamma \\
&= -\frac{1}{\rho r} \frac{\partial}{\partial\theta}\left[\bar{P}_0 - \frac{1}{2}\rho\left(\bar{w}_m^2 + (\bar{w}_u + r\omega)^2\right) + P_s'\right] \\
&\quad + \nu\left[\frac{1}{\sin^2\gamma} \frac{\partial^2}{\partial m^2}(\bar{w}_u + w_u') + \frac{1}{r\sin\gamma} \frac{\partial}{\partial m}(\bar{w}_u + w_u')\right. \\
&\quad + \frac{1}{r^2} \frac{\partial^2}{\partial_\theta^2}(\bar{w}_u + w_u') + \frac{2}{r^2}\sin\gamma \frac{\partial}{\partial_\theta}(\bar{w}_m + w_m') \\
&\quad \left. - \frac{1}{r^2}(\bar{w}_u + w_u')\right] \qquad (10)
\end{aligned}$$

The continuity equation is as follows:

$$\frac{\partial(b\rho r w_m')}{\partial m} + \frac{\partial(b\rho w_u')}{\partial_\theta} = 0 \qquad (11)$$

These equations are solved numerically by introducing a stream function to satisfy the continuity equation.

$$w_m' = \frac{1}{\rho b r} \frac{\partial\psi'}{\partial\theta}$$

and

$$w_u' = -\frac{1}{\rho b} \frac{\partial\psi'}{\partial m} \qquad (12)$$

The kinematic viscosity was considered uniform. Equation (12) was substituted into (9) and (10). Equations (9) and (10) were then expanded in a Fourier series relating to the tangential direction, and were also differentiated with respect to the meridional streamline direction.

The calculation results and experimental results are shown in Figure 20. The same initial conditions were used for the experimental results and for the theoretical calculation. The fluctuation amplitude was normalized with the value at $r/r_2 = 1.03$ for the radial velocity, tangential velocity and the static pressure. The fluctuations of the core flow were adopted as the experimental results. The static pressure became uniform sooner than the velocity for each operating condition, and was very small at $r/r_2 = 1.16$. The fluctuation of the velocity decreased most rapidly for small flowrate conditions. The velocity still fluctuated at $r/r_2 = 1.39$, but the fluctuations became very small at $r/r_2 = 1.69$.

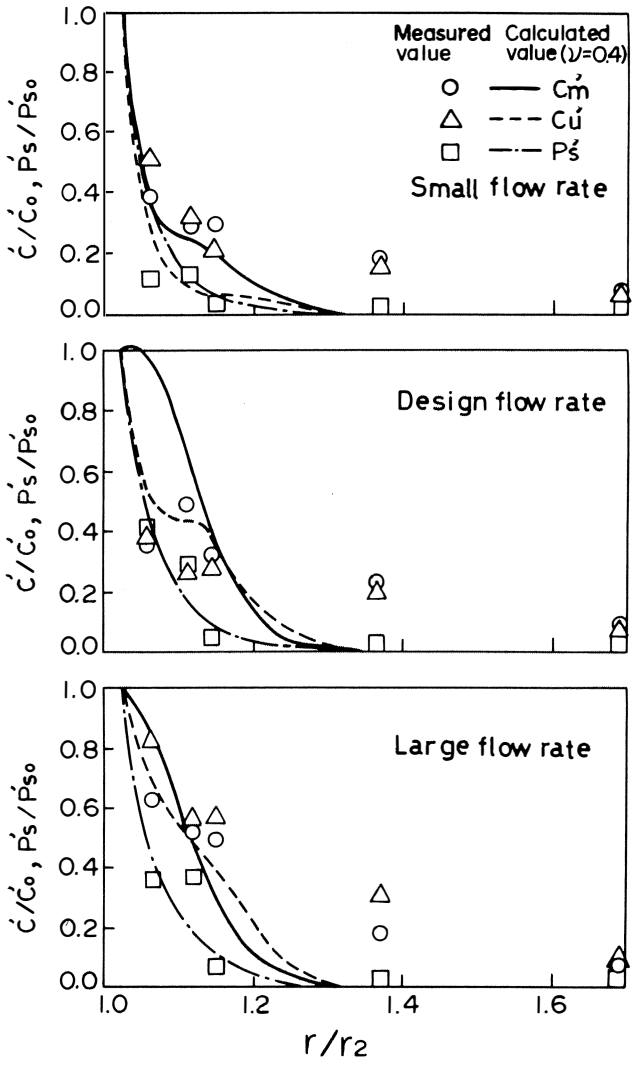

Figure 20. Fluctuation of Velocity and Static Pressure in Curved Vaneless Diffuser.

Distributions of the radial velocity in the blade-to-blade plane at radius ratios $r/r_2 = 1.03$ and 1.14 are shown in Figure 21. At the $r/r_2 = 1.03$ location, the velocity peaked near the blade pressure side, but the velocity was rather uniform except at the shroud and at the blade suction side. A wake existed at the shroud suction side. At the $r/r_2 = 1.14$ station, the peaks of the velocity decayed and the uniform region of velocity increased, because the flow mixed in accordance with the increase of radius. The calculation results of the linearized momentum equations showed that the fluctuation became extremely small at $r/r_2 = 1.2$. There was a significant difference in the velocity fluctuation between theory and experiment at regions more than $r/r_2 = 1.2$.

The linearization of the momentum equations may account for some of the error. Further, the coefficient of viscosity which was used in the calculation did not sufficiently represent the viscosity of the fluid. As for the experimental results, the core flow was not evident in the region of large radius ratios. In such regions, the fluctuation of velocity may be influenced by the three-dimensional boundary layer separation. In the case of the inviscid flow, $\nu = 0$, the fluctuation decreases, according to the theoretical calculation, but the decrease becomes rapid when the viscosity is large.

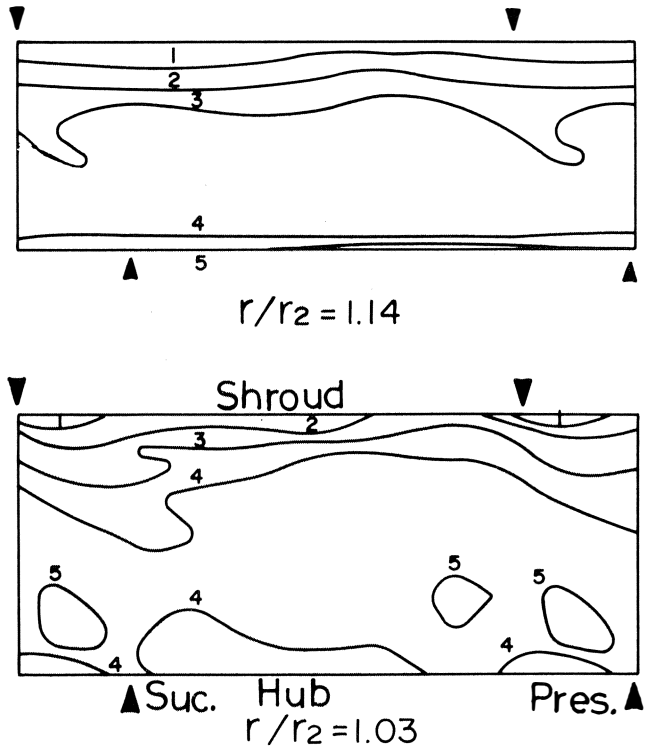

Figure 21. Radial Velocity Distributions in Curved Diffuser.

CONCLUSIONS

A high specific speed mixed flow compressor has been developed and already has been used in practice. The flowrate of this compressor was twice as large as the flowrate through a centrifugal compressor. The pressure ratio was about 2.0.

The size of compressors can be reduced by adopting the mixed flow compressor without any deterioration of performance. The slip factor of the mixed flow compressor is higher than that of centrifugal compressors. This is due to the diagonal pitch angle in a meridional plane.

In the curved diffuser, the flow at the convex wall tends to separate. The diffuser, which is composed of a curved vaneless diffuser and a straight vaned diffuser, showed a high static pressure recovery coefficient by providing the diffuser vanes at the position of the termination of the curvature. Theoretical calculations utilizing linearized momentum equations were used as reference data to determine the position of the diffuser vanes.

NOMENCLATURE

A constant quantity
b width

BL blockage
C absolute velocity
D diameter
g acceleration due to gravity
H head
m coordinate along streamline in meridional plane
N number of revolutions
N_s specific speed, $(m^3/min)^{1/2}$ (rpm) $(m^{-3/4})$
P_s static pressure
P_0 total pressure
Q flow rate
r radius
R_s approximated shroud line curvature
S Cu_2/U_2
U peripheral speed
w relative velocity
Z number of blades
β blade angle measured from tangential line
γ pitch angle in meridional plane from rotor axis
ϵ ratio of wake/passage width
η_{imp} impeller efficiency
η_{stg} stage efficiency
θ coordinate of tangential direction
μ slip factor
ν coefficient of viscosity
ρ density
ϕ flow coefficient
ψ stream function
ω angular velocity

Subscripts

corr corrected quantity
e termination of diffuser wall curvature
h hub
m meridional component
max maximum quantity
opt optimum value
t blade tip
th theoretical
u tangential component
o quantity at $r/r_2 = 1.03$
1 impeller inlet
2 impeller exit
∞ infinite number of blades

Superscripts

$\bar{}$ mean value
$'$ amplitude

BIBLIOGRAPHY

Bammert, K., Rautenberg, M. and Wittekindt, W., "Vaneless Diffuser Flow with Extremely Distorted Inlet Profile," ASME Paper No. 78-GT-47 (1978).

Dean, R. C. and Senoo, Y., "Rotating Wakes in Vaneless Diffusers," ASME Journal of Basic Eng., *82*, pp. 563-574 (September 1960).

Eckardt, D., "Flow Field Analysis of Radial and Backswept Centrifugal Compressor Impellers, Part 1: Flow Measurements Using a Laser Velocimeter," *Performance Prediction of Centrifugal Pumps and Compressors,* ASME, New York, pp. 77-86 (1980).

Inoue, M. and Cumpsty, N. A., "Small Perturbation Analysis of Nonuniform Rotating Disturbances in a Vaneless Diffuser," ASME Paper No. 78-GT-154 (1978).

Kano, F., et al, "Aerodynamic Performance of Large Centrifugal Compressors," Transactions of the ASME, *104*, pp. 796-804 (October 1982).

Sakai, T., Sanbe, M. and Nakayama, T., "Experimental Study on Diffusers for Mixed-Flow Machines," ASME Journal of Engineering for Power, *101*, pp. 281-289 (April 1979).

Senoo, Y. and Ishida, M., "Behavior of Severely Asymmetric Flow in a Vaneless Diffuser," ASME Journal of Engineering for Power, *97* (1975).

Sturge, D. P. and Cumpsty, N. A., "Two-Dimensional Method for Calculating Separated Flow in a Centrifugal Impeller," Journal of Fluids Engineering, pp. 581-597 (December 1972).

Wallace, F. J., Atkey, R. and Whitfield, A., "A Pseudo Three-Dimensional Analysis of Flows in Vaneless Diffusers for Mixed-Flow Compressors," Journal of Mechanical Engineering Science, *17*, pp. 348-356 (June 1975).